Macromolecules **2006,** *39,* 1538−1544

Edge Effects on Thermal Disorder in Laterally Confined Diblock Copolymer Cylinder Monolayers

Matthew R. Hammond[†] and Edward J. Kramer*[,†,‡]

Department of Materials and Department of Chemical Engineering, University of California, Santa Barbara, California 93106

Received September 1, 2005; Revised Manuscript Received November 27, 2005

ABSTRACT: The edges of channels etched into topographically patterned substrates impart orientational order to monolayers of poly(styrene-*b*-2-vinylpyridine) cylinders. Quantitative measures of orientational order as well as defect densities are presented for cylinder arrays confined in channels of width varying between 1 and 3 μm, with little, if any, difference observed between these different channel widths. As the temperature is raised, the cylinder monolayers undergo a nematic-to-isotropic disordering transition. However, above this transition temperature, orientational order is retained within several cylinder repeat spacings next to the channel edges (distances significantly less than the channel widths considered here). This effect arises from an effective repulsion of defects from those edges, as confirmed by position-dependent defect density measurements.

Introduction

The self-assembling properties of block copolymers make them potentially very useful as low-cost, large-area templates for the fabrication of nanoscale structures,[1,2] enabling a variety of magnetic storage and semiconductor applications.[3−5] For the most demanding applications, however, exquisite control over the domain orientation and registry in the copolymer thin film is required. In the case of copolymer cylinders lying in the film plane, various strategies have been employed to overcome the tendency of the cylinders to form the characteristic fingerprint-like pattern, including the use of electric fields,[6,7] directional crystallization,[8] the application of shear,[9] and graphoepitaxy, an approach first applied to block copolymer spheres[10] and later applied to cylinders,[11−14] in which shallow channels prepatterned in the substrate force the copolymer domains into registry with the topographic features.

We have recently reported on the equilibrium temperature dependence of order in monolayers of polystyrene-*b*-poly(2-vinylpyridine) (PS−PVP) cylinders confined within long channels of 2 μm width, finding that the order obtained in the monolayer is a strongly decreasing function of increasing temperature,[14] in agreement with theory.[15] At low temperatures (well below the copolymer's bulk order−disorder transition temperature (ODT)), this is primarily due to the thermal generation of dislocations, which were found to occur with a density

$$n_D \approx a_c^{-2} \exp(-E_D/k_BT) \qquad (1)$$

where a_c is the dislocation core radius and E_D is the energy associated with the creation of a dislocation. It has been noted that block copolymer cylinder monolayers possess the symmetry of a two-dimensional smectic liquid crystal.[16,17] However, in two dimensions, the long-range translational order that is characteristic of the smectic phase is possible only at $T = 0$; at finite temperatures thermal fluctuations and thermally generated dislocations cause the translational order in 2D smectic systems to be short-ranged.[15] Thus, the locally layered phase observed at low temperatures is most properly termed a nematic (characterized by short-range translational order and quasi-long-range orientational order). In the case of copolymer cylinder monolayers, the local normal to the cylinders plays the role of the nematic director. At these low temperatures, disclinations in the confined cylinder arrays were rarely observed and, when observed, occurred only as "close pairs", in which the component $\pm^1/_2$ disclinations were separated by ~1.5 repeat spacings or less. At higher temperatures, however, a higher density of both dislocations and unbound disclinations were observed, reducing the orientational order of the cylinders to short-range and creating an "isotropic" phase which we speculate is really the two-dimensional analogue to the 3D disordered phase in which local volume fraction fluctuations give rise to a diffuse scattering peak. The phase progression smectic → nematic → isotropic is analogous to the crystal → hexatic → liquid-phase behavior observed in 2D hexagonal arrays[18−20] with the exception that the solid phase in the striped system exists solely at $T = 0$.[15]

In this paper we describe the behavior of our graphoepitaxially confined cylinder monolayer system near the channel edges. Sibener et al. have observed the mechanism by which polystyrene-*b*-poly(ethylene-*alt*-propylene) (PS−PEP) cylinder multilayers align within patterned channels, showing that 1−2 cylinders align with the channel walls very rapidly.[13] On continued annealing, this cylinder alignment ripened across the entire channel width at random locations along the channel length, and these aligned domains grew at the expense of unoriented regions until the alignment persisted along the entire channel width and length. Their early-time observation suggests a strong stabilization of aligned cylinders near the channel edges. Segalman et al. observed stabilization of the hexatic phase of a monolayer of PS−PVP spheres near the edges of 15 μm wide channels, whereas in the center of the channels the spheres were in the liquid state.[21] Here, we report a similar stabilization of cylinder order near the confining edges, although the stabilization only persists over distances on the order of several repeat spacings. This stabilization takes the form of an increased alignment of the cylinders near the walls and a corresponding depletion of defects near the walls. We also report measurements of cylinder order within channels of three different widths,

---

* To whom correspondence should be addressed. E-mail: edkramer@mrl.ucsb.edu.

[†] Department of Materials.

[‡] Department of Chemical Engineering.

10.1021/ma051912u CCC: $33.50

namely 1, 2, and 3 μm, and find that the cylinder order observed is nearly independent of channel width.

Experimental Section

Diblock Copolymer. Polystyrene-*b*-poly(2-vinylpyridine) (PS−PVP) with overall molecular weight $M_n = 26\,000$, polydispersity index 1.07, and mole fraction of PVP mers $f_{PVP} = 0.25$ was synthesized via anionic polymerization as previously described.[14] This copolymer orders in bulk into hexagonally packed cylindrical PVP core domains in a PS matrix, with a nearest-neighbor spacing of $a = 22$ nm. The bulk ODT for this copolymer was measured to be ∼212 °C.[14]

Substrate Fabrication. Plasma-enhanced chemical vapor deposition was employed to deposit 20 nm thick silicon oxide layers onto native-oxide covered silicon wafers. These layers were patterned with a series of 500 μm long, 20 nm deep channels via standard photolithography and etching in an inductively coupled CHF_3 plasma. Channel widths of 1, 2, and 3 μm were produced. Prior to copolymer film deposition, the patterned substrates were cleaned thoroughly to remove photoresist and etch residues.[14]

Film Deposition, Annealing, and Imaging. PS−PVP films were spin-coated from dilute (∼1%) toluene solution with a thickness such that, upon annealing, the channels contained a monolayer of copolymer cylinders (lying atop a brush layer), while the mesas separating the channels were covered only with the brush layer.[14,22] Samples were annealed (within a high-vacuum furnace operating at base pressures better than 10^{-6} mbar) at 220 °C for 1 h, cooled slowly (∼1 °C/min) to a given temperature, held at that temperature for 4 h, and quickly quenched below the PS−PVP glass transition temperature ($T_g \approx 100$ °C). We report here results from samples whose final annealing temperatures were 205, 200, 195, 190, 185, 180, 170, and 150 °C. As we have shown previously, these thermal treatments yield copolymer structures which can be regarded for practical purposes as being at equilibrium.[14]

To image the PS−PVP microstructure, the copolymer films were etched with the O^{2+} ion beam of a Physical Electronics 6650 dynamic secondary ion mass spectrometer, as previously described.[14] This etching results in 1−2 nm deep pits corresponding to the PVP cylinder cores, which were imaged using a Digital Instruments MultiMode scanning force microscope (SFM), operated in tapping mode. Images were corrected for stretching or compression along the SFM slow scan direction as necessary.[14,18]

Defect Counting. Defect densities were determined from many 1 μm^2 images in which the cylinder cores were carefully traced, facilitating the identification of dislocations and disclinations. The positions of the individual defects relative to the channel edges, and to each other, were thus easily recorded. In the case of disclinations, the densities of $\pm^1/_2$ disclinations were found to be essentially equal, as expected, and therefore we only report $+^1/_2$ disclination densities here.

Calculation of Orientational Correlation Functions. The image processing protocols we have used to determine the local cylinder orientation, based on the methods of Harrison et al.,[17] have been previously reported.[14] Briefly, the orientation field $\theta(\mathbf{r})$ of the cylinder normals was determined by calculating the local gray scale intensity gradients within a given processed SFM image, with the angle θ defined relative to the image horizontal (perpendicular to the channel edges). Subsequently, the orientational order parameter field $\psi_2(\mathbf{r})$ was calculated according to

$$\psi_2(\mathbf{r}) = \exp[2i\theta(\mathbf{r})] \tag{2}$$

where the factor of 2 accounts for the 2-fold degeneracy of the cylinder normal direction. This order parameter field could then be used to find the orientational correlation function, $g_2(\mathbf{r})$, as follows.

$$g_2(\mathbf{r}) = \langle \psi_2^*(\mathbf{0})\psi_2(\mathbf{r})\rangle \tag{3}$$

Here the angular brackets imply an averaging over all pairs of points, and we have employed a subtle shift in notation such that in eq 3 $\mathbf{r}$ represents the vector separating the two points being correlated. We report below simply the azimuthal average of this function, $g_2(r)$. Additionally, $\psi_2(\mathbf{r})$ was correlated with the orientation of the channel edge, specifically as a function of the distance from that edge, viz.

$$g_{2,\mathrm{edge}}(z) = \sum_x [\psi_{\mathrm{edge}}^* \psi_2(x,z)] \tag{4}$$

where $\psi_{\mathrm{edge}} = \exp[2i(0)] = 1$ since the angle that the edge normal makes with the image horizontal is 0.[23] The result is normalized by the number of correlation pairs N involved in the calculation. Finally, we calculate the z-dependent one-point correlation functions in both the x and z directions

$$\Psi_z(z) = \frac{1}{N}\sum_x \psi_2^*(x,z)\cdot\psi_2(x,z+a) \tag{5a}$$

$$\Psi_x(z) = \frac{1}{N}\sum_x \psi_2^*(x,z)\cdot\psi_2(x+a,z) \tag{5b}$$

where a is the cylinder−cylinder repeat spacing, which give measures of the orientational correlation between neighboring cylinders (z direction, eq 5a) and between adjacent segments along the length of a given cylinder (x direction, eq 5b). The Ψ functions are normalized by the number of correlation pairs involved in the calculation, N.

Results and Discussion

PS−PVP cylinder arrays confined within 1−3 μm channels show excellent alignment with the channel edges when cooled from above the 3D ODT to sufficiently low final annealing temperatures. Figure 1a shows an SFM phase image of such a sample, annealed at a final temperature of 150 °C within a 2 μm wide channel. The cylinders are clearly aligned with the channel edge (visible at the extreme left of the image). This alignment extends over the entire channel width (not shown), and similar results are obtained for channel widths of 1 and 3 μm. In samples annealed at 180 °C (Figure 1b), the cylinders also adopt the channel edge orientation, although a higher density of dislocations is present. At 195 °C (Figure 1c), a temperature just above the nematic−isotropic transition temperature, T_{NI}, the cylinders in the center of the well no longer adopt the edge orientation. However, in a narrow region directly adjacent to the edge, the PS−PVP cylinders are aligned with the edge.

These observations are quantified by analyzing the cylinder-edge orientational correlation function, $g_{2,\mathrm{edge}}(z)$, as a function of temperature, as shown in Figure 2a. Below 190 °C, $g_{2,\mathrm{edge}}$ remains nearly constant at ∼0.9 across the entire channel (cross and square symbols). At 190 °C (open circle symbols), just below T_{NI}, $g_{2,\mathrm{edge}}$ remains nearly constant (∼0.8) across the channel width but is enhanced in a region within 7−10 repeat spacings from the edge. At temperatures above T_{NI} (star and open diamond symbols), the cylinders are essentially uncorrelated with the edge direction, except in a region within 7−10 repeat spacings from the edge. Similar trends are evident in the one-point orientational correlation functions, Ψ_z (Figure 2b) and Ψ_x (Figure 2b). These functions, in practice, measure the cosine of the difference in orientation angle between points separated by one repeat distance in the z- and x-direction, respectively, averaged over all points in the image. An image with perfectly uniform orientation would yield $\Psi_z = \Psi_x = 1$. As evidenced in Figure 2b, at temperatures above T_{NI} (star and open diamond symbols), Ψ_z is clearly enhanced in a region directly adjacent to the well edge, extending only several repeat spacings. Similar

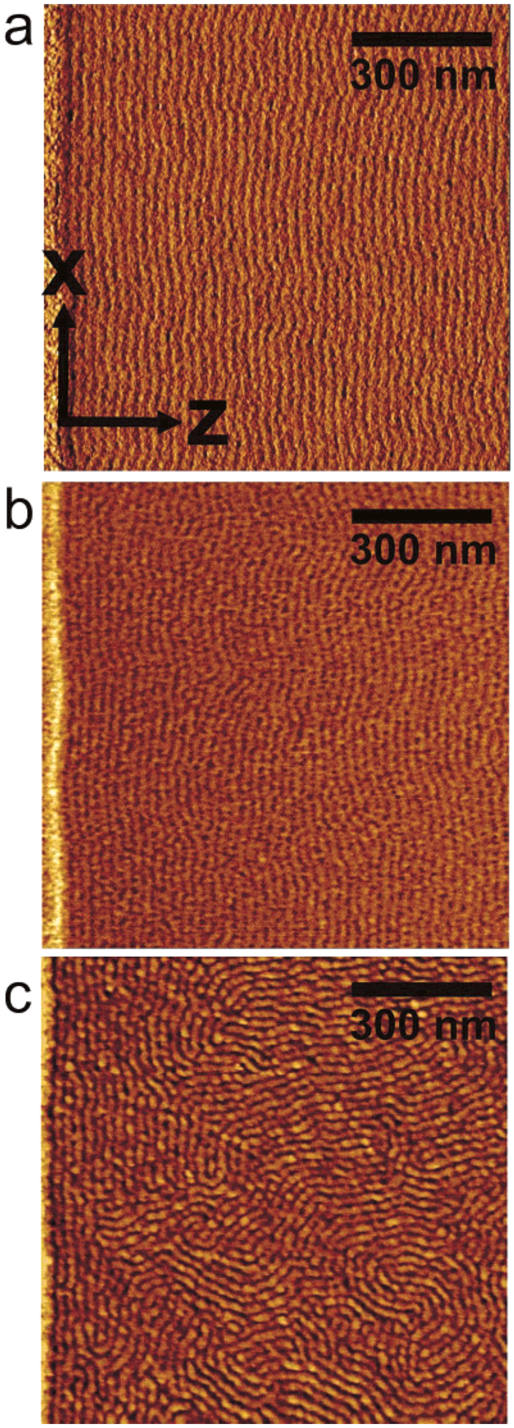

Figure 1. Tapping mode SFM phase images of cylinder arrays confined within 2 μm wide, 20 nm deep channels. One edge of the channel is visible on the left-most edges of the images. The samples were annealed as described in the Experimental Section, with final temperatures of 150 (a), 180 (b), and 195 °C (c). A set of axes is included in (a) marking the notational conventions used in this work; the *z*-direction is that of the average cylinder normal (in the nematic regime), and the *x*-direction runs parallel to the cylinders.

behavior is exhibited in Ψ_x. It is interesting to note, however, that the value of Ψ_x in the ordered samples (lower temperatures) is significantly less than that of Ψ_z. The elastic properties of a (3D) smectic are governed by the constants, K_1 and B, the Frank constant for bending the layers (due to molecular splay of the polymer chains) and the layer compressional modulus, respectively. Harrison and co-workers, studying monolayers of polystyrene-*b*-polyisoprene cylinders, showed that the distortional energy associated with layer bending was on the order of 10^3 times lower than that for layer compression or dilation.[17] That is, introducing splay between adjacent cylinders (which requires layer compression and dilation) is more difficult than bending a cylinder along its axis—consistent with our observation that $\Psi_z > \Psi_x$ for samples in the nematic regime. This fact can be easily observed in a pseudo-color rendering of the orientation field, $\theta(\mathbf{r})$, for an image of a well-ordered sample shown in Figure 3. A brief inspection shows that cylinder orientations are more highly correlated in the direction perpendicular to the cylinders than in the parallel direction.

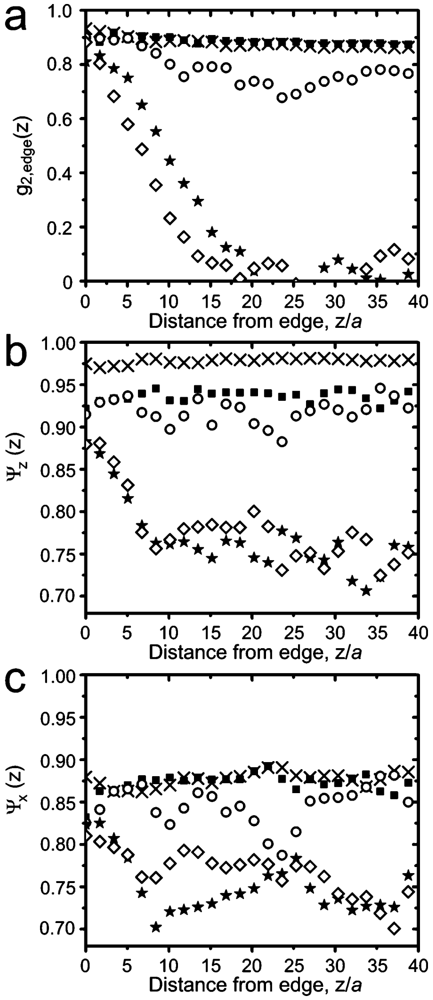

Figure 2. (a) Orientational correlation functions with respect to the well edge, as a function of reduced distance from the edge, for the following temperatures: 150 °C (×'s), 180 °C (squares), 190 °C (open circles), 195 °C (stars), and 200 °C (open diamonds). (b, c) One-point orientational correlation functions, Ψ_z (b) and Ψ_x (c), as a function of reduced distance from the well edge for the same temperatures as in (a).

Short-Ranged Repulsion of Defects from Well Edges. Our previous experiments, in agreement with theory, showed that defects mediate the disordering of the confined cylinder arrays.[14] The stabilization of cylinder order near the channel edges, even at high temperatures, coincides with an exclusion of defects from a region near those edges, as can be observed in parts a and b of Figure 4, plots of dislocation density and $+{}^1/_2$ disclination density, respectively, as a function of distance from the channel edge for temperatures of 180 °C (squares), 190 °C (open circles), and 195 °C (stars). At temperatures lower than 180 °C, the overall dislocation density was too low to get reasonable statistics for data of this type. The same is true for the

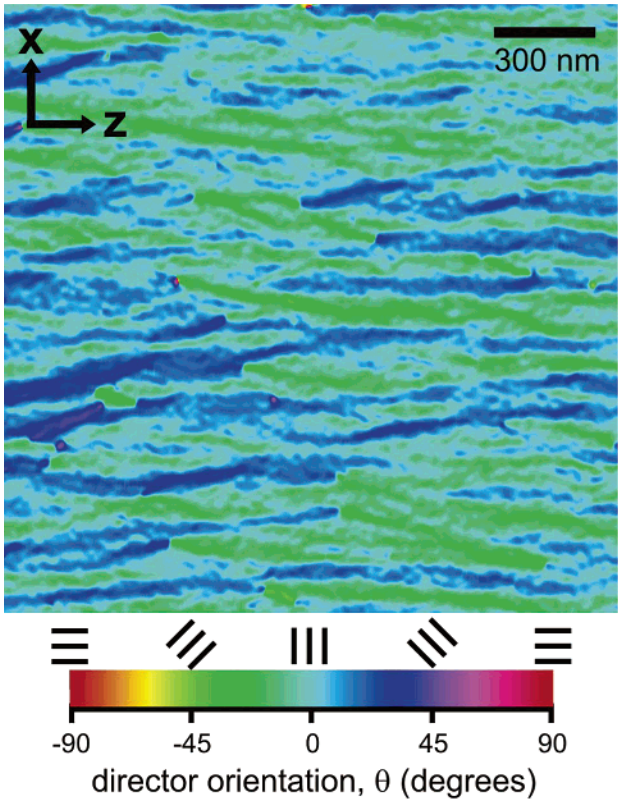

Figure 3. Pseudo-color map of the cylinder normal orientation field, $\theta(\mathbf{r})$, for an image of a sample annealed at a final temperature of 150 °C within a 2 μm channel. Regions of correlated color (orientation) are highly elongated in the z-direction, perpendicular to the cylinders, indicating that bending along the length of the cylinders is associated with much less distortional energy than introducing splay between adjacent cylinders.

disclination density below 190 °C. Figure 4a shows that for the three temperatures represented dislocations are strongly excluded from the first ~2−4 repeat spacings next to the channel edge. Beyond that distance, the dislocation density quickly saturates to a near-constant value. Similar behavior is observed in the disclination density plot in Figure 4b, although disclinations are evidently repelled from a slightly larger zone near the edge of ~4−8 repeat spacings.

Pershan has calculated the stress fields associated with dislocations within layered systems[24] such as the PS−PVP cylinder monolayers studied here and the resulting forces between dislocations and between dislocations and solid surfaces. In the latter case, a dislocation should be repelled from a solid surface as if from an "image dislocation" of the same Burgers vector located an equal distance on the opposite side of the surface (as shown, for example, as dislocations α and α′ in Figure 5a). For the general case of two dislocations, α and β, as in Figure 5b, separated by (x, $z_\beta - z_\alpha$), Pershan gives the z-component of the force (per unit length) exerted on dislocation α due to the strain field of dislocation β, $f_z^{\alpha,\beta}$, as

$$f_z^{\alpha,\beta} = \frac{s_{\alpha,\beta}a^2B}{8\lambda(\pi\zeta)^{1/2}}\frac{\zeta}{|\zeta|^2}\left[\frac{\xi^2}{2\zeta} - 1\right]\exp\left(-\frac{\xi^2}{4|\zeta|}\right) \qquad (6)$$

where $s_{\alpha,\beta} = -1$ if α and β have opposite Burgers vectors (as is drawn in Figure 5b) and $s_{\alpha,\beta} = +1$ if α and β have the same Burgers vector, $\lambda \equiv (K_1/B)^{1/2}$ is the "penetration depth", and $\xi \equiv x/\lambda$ and $\zeta \equiv (z_\beta\text{-}z_\alpha)/\lambda$.[24] The energy per unit length of an isolated dislocation in a smectic liquid crystal is

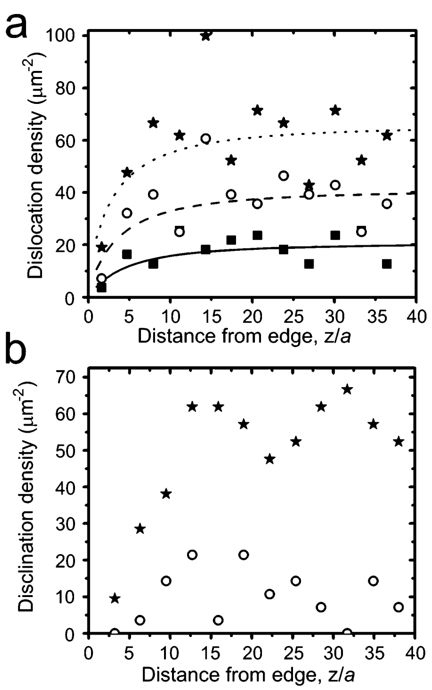

Figure 4. Dislocation (a) and $+^1/_2$ disclination (b) densities as a function of distance from the channel edge for PS−PVP monolayers confined within 2 μm wide channels, annealed at 180 °C (squares), 190 °C (open circles), and 195 °C (stars). Note that at 180 °C the overall disclination density is too low to allow statistically significant data to be obtained. In (a), the fits are to the function $C' \exp[-\Phi_{\text{pair}}(z_\alpha)/k_BT]$ using the values for C' and B described in the text.

$$\epsilon_D = \frac{\lambda b^2}{2a_c}B + \epsilon_c \qquad (7)$$

where b is the magnitude of the Burgers vector and ϵ_c represents the contribution of the local perturbations at the dislocation core of radius a_c.[25] The excess elastic energy (above and beyond that described in eq 7) of an isolated dislocation located a distance z_α from the wall (the case illustrated in Figure 5a), obtained by integrating eq 6, is

$$\Phi(z_\alpha) = \frac{1}{8}a^2B\left(\frac{\lambda}{2\pi}\right)^{1/2}{z_\alpha}^{-1/2} \qquad (8)$$

(per unit length).[24] Adding eqs 7 and 8 and multiplying by the thickness of the cylinder monolayer (~19 nm) gives the energy, E_D, that should be used in eq 1 to predict the dislocation density. The form $n_D \sim \exp(-{z_\alpha}^{-1/2})$ thus obtained would imply a much longer-range repulsion of dislocations from the channel edge than what we observe in Figure 4a.

However, the pairing of dislocations with opposite Burgers vectors, as shown schematically in Figure 5b, can dramatically reduce the overall strain field relative to that created by individual dislocations. To estimate the repulsion of such a dislocation pair from the channel wall, all of the various interactions must be included: α−α′, β−β', α−β, β−α, α−β', and β−α′ (by symmetry, β−α = α−β and β−α′ = α−β').

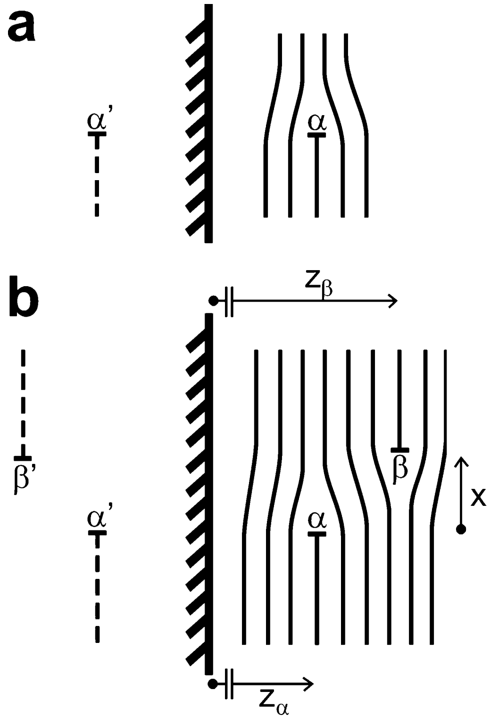

Figure 5. Schematic representations (cylinder cores represented by dark lines) of dislocation configurations described in the text. In (a), an isolated dislocation at position α is repelled from a hard wall (vertical line with hash marks) by an image force from a dislocation at α′. In (b), a pair of oppositely signed dislocations interact to decrease the overall strain field relative to that of two isolated dislocations, thus reducing their repulsion from the well edge. The conventions used in the text for distances of the dislocations from the edge, z_α and z_β, as well as the distance between them in the direction parallel to the edge, x, are indicated.

We obtain, using the substitutions $\zeta_\alpha = z_\alpha/\lambda$, $\zeta_\beta = z_\beta/\lambda$, and $\xi = x/\lambda$

$$\Phi_{\text{pair}}(\zeta_\alpha,\zeta_\beta,\xi) = \frac{1}{8}\frac{a^2B}{\pi^{1/2}}\left[\frac{1}{(2\zeta_\alpha)^{1/2}} + \frac{1}{(2\zeta_\beta)^{1/2}} - \frac{2}{|\zeta_\alpha - \zeta_\beta|^{1/2}}\exp\left\{\frac{-\xi^2}{4|\zeta_\alpha - \zeta_\beta|}\right\} - \frac{2}{(\zeta_\alpha + \zeta_\beta)^{1/2}}\exp\left\{\frac{-\xi^2}{4(\zeta_\alpha + \zeta_\beta)}\right\}\right] \quad (9)$$

By looking at the relative positions of pairs of dislocations with opposite Burgers vector in the sample represented by the square points in Figure 4a (annealed at 180 °C), we found that such pairs were separated on average by $x \approx 2a$ and $z_\beta - z_\alpha \approx 4.5a$.

Combining eqs 7 and 9 with eq 1, using the estimate[26] $\lambda = 0.1a$, and setting $x = 2a$ and $z_\beta = z_\alpha + 4.5a$, we were able to fit the data from Figure 4a via

$$n_{\text{D}}(z_\alpha) = C' \exp[-\Phi_{\text{pair}}(z_\alpha)/k_{\text{B}}T] \quad (10)$$

with only two adjustable parameters, namely C' and B. The parameters used for the fits are [C', B, temperature] [17, 60 kPa, 180 °C—solid line], [35, 50 kPa, 190 °C—dashed line], and [58, 40 kPa, 195 °C—dotted line]. It is logical that B should decrease with increasing temperature, typically linearly within the nematic regime and faster in the vicinity of T_{NI}. Similarly, the increase in C' with increasing temperature reflects the fact that C' incorporates a term $\exp[-B(T)/k_{\text{B}}T]$ from the dislocation self-energy (eqs 7 and 1). We also note that these values of the compressional modulus are ~4–6 times less than those estimated previously through self-consistent-field theory (SCFT) simulations.[14] However, our previous estimate of the dislocation self-energy, obtained from fitting experimental defect density data, implied that the SCFT results overestimated B, perhaps by as much as a factor of 3.[14] Given the present uncertainties (both experimental and in estimates of quantities such as a_{c} and λ), we believe the values of B used for these fits to be reasonable. Finally, we note that $\pm^1/_2$ disclination pairs can be treated to a first approximation as "super dislocations" with Burgers vectors equal to some multiple of the repeat distance.[14] Thus, the above arguments should also apply to the functional form with which disclination pairs are repelled from the channel edges.

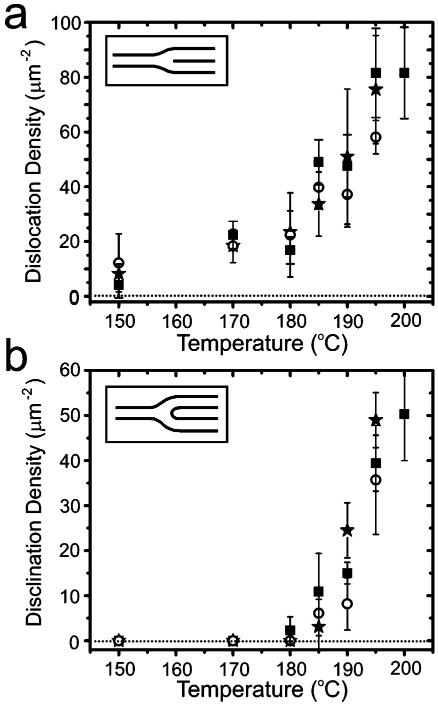

Figure 6. Dislocation (a) and $+^1/_2$ disclination (b) densities as a function of final annealing temperature for PS–PVP cylinder arrays confined within channels of width 1 μm (stars), 2 μm (squares), and 3 μm (open circles), measured from the center regions of the respective channels. In the defect schematics shown here, the black lines represent cylinder cores.

Properties within Different Channel Widths. Given that thermal defect generation and disclination unbinding are responsible for the nematic–isotropic cylinder disordering process[14] and that at sufficiently high defect densities pairs or other groupings of defects can be configured such as to minimize the overall lattice strain (causing them to be excluded only from a narrow region next to the channel edge), it should perhaps be unsurprising that the nematic–isotropic transition temperature is quite insensitive to the channel width.[27] Figure 6 displays dislocation (Figure 6a) and $+^1/_2$ disclination (Figure 6b) densities measured from the center regions of cylinder arrays confined within channels of 1 μm (stars), 2 μm (squares), and 3 μm (open circles) width as a function of final annealing temperature. Very little significant difference is discernible in these data with respect to the different channel widths. Similar invariability in T_{NI} is suggested by the azimuthally averaged orientational correlation function ($g_2(r)$) results presented in Figure 7. The cylinder nematic-to-isotropic transition is indicated by a change from algebraic decay in $g_2(r)$ (yielding a straight line fit on a log–log scale, as seen in Figure 7a) to exponential decay in $g_2(r)$ (which is easily viewed as a straight line fit on a semilog

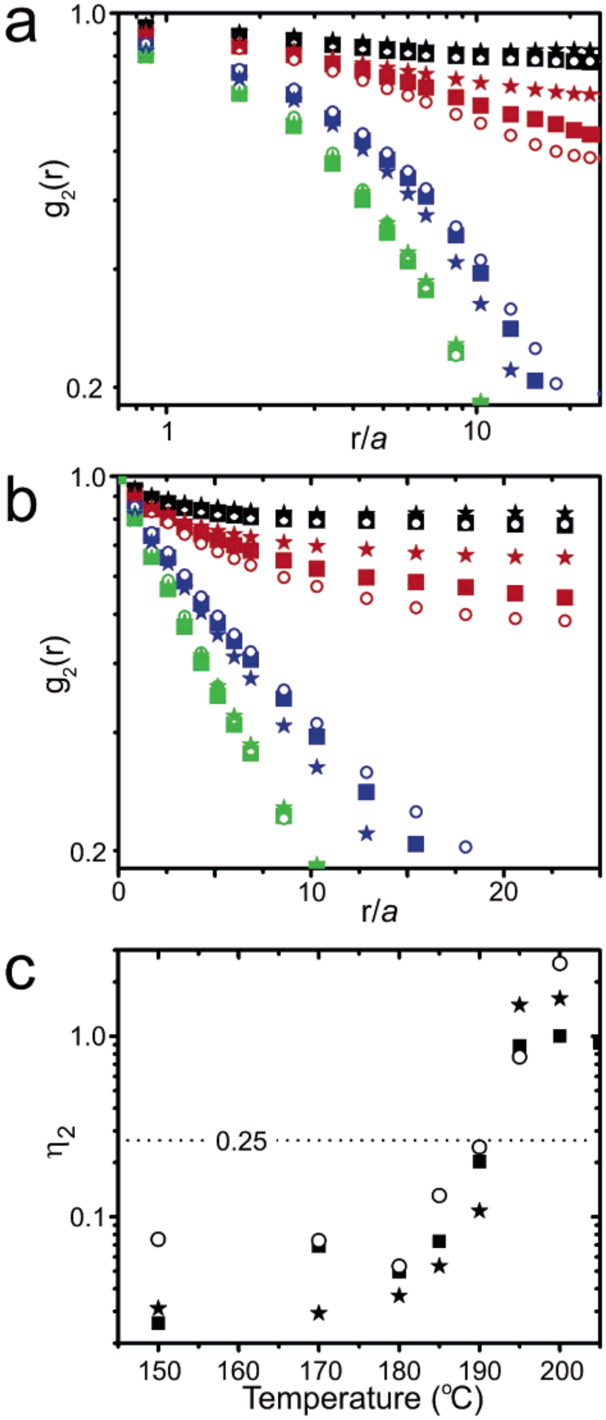

Figure 7. Azimuthally averaged orientational correlation function results for samples annealed at 180 °C (black symbols), 190 °C (red symbols), 195 °C (blue symbols), and 200 °C (green symbols), plotted on a log−log scale (a) and a semilog scale (b). Qualitatively similar results are obtained at all temperatures for all three channel widths: 1 μm (stars), 2 μm (squares), and 3 μm (open circles). Specifically, algebraic decay is observed at 190 °C and below in (a), and exponential decay in $g_2(r)$ is observed for 195 and 200 °C in (b). Algebraic decay exponents, $\eta_2(T)$, obtained from fitting the data in (a) are plotted in (c) for the three channel widths. The dotted line at $\eta_2 = {}^1/_4$ represents the condition set forth in ref 15 for the nematic−isotropic transition. For all channel widths, η_2 increases steadily over the temperature range plotted here, exceeding ${}^1/_4$ somewhere between 191 and 193 °C.

scale, Figure 7b). At all temperatures, qualitatively identical behavior is obtained between the different channel widths; the transition from algebraic to exponential decay of $g_2(r)$ occurs between 190 °C (red symbols) and 195 °C (blue symbols) for all channel widths. Fitting the data in Figure 7a to algebraic decay, i.e.

$$g_2(r) \sim r^{-\eta_2(T)} \tag{11}$$

yields the algebraic decay exponent, η_2, which is predicted to exceed a value of ${}^1/_4$ at the N−I transition temperature.[15] These values are plotted in Figure 7c, showing that η_2 exceeds ${}^1/_4$ (dotted line) somewhere between 191 and 193 °C for all channel widths. These data may indicate a slight depression (of ∼1−2 °C) in T_{NI} as the channel width is increased from 1 to 3 μm. However, given the scatter in the data, we hesitate to attach much significance to this.

Conclusion

The channel edges that confine the PS−PVP arrays studied here impart orientational order to the copolymer cylinders. Below the nematic-to-isotropic transition temperature, that orientational order persists across the entire width of channels up to 3 μm wide, with similar defect densities and measures of orientational order observed at a given temperature for all three channel widths. Above the nematic-to-isotropic transition temperature, however, the orientational order imparted by the channel edges dies out after several cylinder repeats. This local stabilization of ordered cylinders near the channel edges arises from the repulsion of defects from the edge. Qualitative agreement with the form of the measured defect density as a function of distance from the confining edge is obtained using model equations for the strain fields associated with dislocation pairs and rough estimates for the relevant physical properties of the system.

Acknowledgment. This work was supported by the National Science Foundation DMR-Polymers Program under Grant DMR03-07233 and made use of MRL Central Facilities supported by the NSF MRSEC Program under Award DMR00-80034. We gratefully acknowledge several useful discussions with Professor David Nelson. M.R.H. thanks Professor Matthew Turk, Gila Stein and Alexander Hexemer for technical assistance regarding image analysis.

References and Notes

(1) Park, M.; Harrison, C.; Chaikin, P. M.; Register, R. A.; Adamson, D. H. *Science* **1997**, *276*, 1401−1404.
(2) Park, C.; Yoon, J.; Thomas, E. L. *Polymer* **2003**, *44*, 6725−6760.
(3) Naito, K.; Hieda, H.; Sakurai, M.; Kamata, Y.; Asakawa, K. *IEEE Trans. Magn.* **2002**, *38*, 1949−1951.
(4) Black, C. T.; Guarini, K. W.; Zhang, Y.; Kim, H. J.; Benedict, J.; Sikorski, *IEEE Electron Device Lett.* **2004**, *25*, 622−624.
(5) Thurn-Albrecht, T.; Schotter, J.; Kastle, C. A.; Emley, N.; Shibauchi, T.; Krusin-Elbaum, L.; Guarini, K.; Black, C. T.; Tuominen, M. T.; Russell, T. P. *Science* **2000**, *290*, 2126−2129.
(6) Morkved, T. L.; Lu, M.; Urbas, A. M.; Ehrichs, E. E.; Jaeger, H. M.; Mansky, P.; Russell, T. P. *Science* **1996**, *273*, 931−933.
(7) Mansky, P.; DeRouchey, J.; Russell, T. P.; Mays, J.; Pitsikalis, M.; Morkved, T.; Jaeger, H. *Macromolecules* **1998**, *31*, 4399−4401.
(8) Park, C.; De Rosa, C.; Thomas, E. L. *Macromolecules* **2001**, *34*, 2602−2606.
(9) Angelescu, D. E.; Waller, J. H.; Adamson, D. H.; Deshpande, P.; Chou, S. Y.; Register, R. A.; Chaikin, P. M. *Adv. Mater.* **2004**, *16*, 1736−1740.
(10) Segalman, R. A.; Yokoyama, H.; Kramer, E. J. *Adv. Mater.* **2001**, *13*, 1152−1155.
(11) Sundrani, D.; Sibener, S. J. *Macromolecules* **2002**, *35*, 8531−8539.
(12) Sundrani, D.; Darling, S. B.; Sibener, S. J. *Langmuir* **2004**, *20*, 5091−5099.
(13) Sundrani, D.; Darling, S. B.; Sibener, S. J. *Nano Lett.* **2004**, *4*, 273−276.
(14) Hammond, M. R.; Cochran, E.; Fredrickson, G. H.; Kramer, E. J. *Macromolecules* **2005**, *38*, 6575−6585.
(15) Toner, J.; Nelson, D. R. *Phys. Rev. B* **1981**, *23*, 316−334.

(16) Harrison, C.; Adamson, D. H.; Cheng, Z. D.; Sebastian, J. M.; Sethuraman, S.; Huse, D. A.; Register, R. A.; Chaikin, P. M. *Science* **2000**, *290*, 1558−1560.

(17) Harrison, C.; Cheng, Z. D.; Sethuraman, S.; Huse, D. A.; Chaikin, P. M.; Vega, D. A.; Sebastian, J. M.; Register, R. A.; Adamson, D. H. *Phys. Rev. E* **2002**, *66*, 011706.

(18) Segalman, R. A.; Hexemer, A.; Hayward, R. C.; Kramer, E. J. *Macromolecules* **2003**, *36*, 3272−3288.

(19) Marcus, A. H.; Rice, S. A. *Phys. Rev. E* **1997**, *55*, 637−656.

(20) Murray, C. A.; Vanwinkle, D. H. *Phys. Rev. Lett.* **1987**, *58*, 1200−1203.

(21) Segalman, R. A.; Hexemer, A.; Kramer, E. J. *Phys. Rev. Lett.* **2003**, *91*, 196101.

(22) Segalman, R. A.; Schaefer, K. E.; Fredrickson, G. H.; Kramer, E. J.; Magonov, S. *Macromolecules* **2003**, *36*, 4498−4506.

(23) Harrison et al. have reported preliminary $g_{2,\mathrm{edge}}$ data for a somewhat similar system of block copolymer cylinders confined within long islands that formed on top of patterned silicon mesas 4 μm in width. Harrison, C.; Dagata, J. A.; Adamson, D. H. In *Developments in Block Copolymer Science and Technology*; Hamley, I. W., Ed.; Wiley: Chichester, 2004; pp 295−323.

(24) Pershan, P. S. *J. Appl. Phys.* **1974**, *45*, 1590−1604.

(25) Chandrasekhar, S.; Ranganath, G. S. *Adv. Phys.* **1986**, *35*, 507−596.

(26) Amundson, K.; Helfand, E. *Macromolecules* **1993**, *26*, 1324−1332.

(27) We note that the channel widths studied here are significantly larger than the range of the defect repulsion from the channel edges. Presumably, if the channel width is on the order of (twice) this distance, one should observe the stabilization of ordered cylinders across the entire channel width even at very high temperatures.

MA051912U